Integrative Modelling of Signalling Network Dynamics Identifies Cell Type-selective Therapeutic Strategies for FGFR4-driven Cancers

Sung-Young Shin[1,2,*], Nicole J Chew[1,2,*], Milad Ghomlaghi[1,2], Anderly C Chüeh[1,2], Lan K. Nguyen[1,2,#] and Roger J Daly[1,2,#]

[1]Cancer Program, Biomedicine Discovery Institute, Monash University, Melbourne, VIC 3800, Australia.
[2] Department of Biochemistry and Molecular Biology, Monash University, Melbourne, VIC 3800, Australia.

* These authors contributed equally to the work
[#] Correspondence: roger.daly@monash.edu; lan.k.nguyen@monash.edu

Abstract

Oncogenic FGFR4 signalling represents a potential therapeutic target in many cancer types, including triple negative breast cancer (TNBC) and hepatocellular carcinoma (HCC). However, resistance to single-agent therapy directed at FGFR4 remains a major challenge, prompting the need to identify more effective combinatorial therapeutic strategies. Here, we integrated computational network modelling and experimental validation to characterise dynamic reprogramming of the FGFR4 signalling network in TNBC following FGFR4 kinase inhibition. We found that AKT, which signals downstream of FGFR4, displayed a rapid and potent reactivation following FGFR4 targeting. Through model-based simulation and systematic prediction of the effect of co-targeting specific network nodes, we predicted, and validated experimentally, strong synergism of co-targeting FGFR4 and particular ErbB kinases or AKT, but not the upstream kinase PI3K. Further, incorporation of protein expression data from hundreds of cancer cell types enabled us to adapt our model to other diverse cellular contexts, leading to the prediction that while AKT rebound occurs frequently, it is not a general phenomenon. Instead, ERK is reactivated in a subset of cell types, including the FGFR4-driven HCC cell line Hep3B. This was subsequently corroborated, and moreover, co-targeting FGFR4 and MEK in Hep3B cells markedly enhanced inhibition of cell proliferation. Overall, these findings provide novel insights into the dynamics of drug-induced network remodelling in cancer cells, highlight the impact of protein expression heterogeneity on network response to targeted therapy and identify candidate cell type-selective combination treatments for FGFR4-driven cancer.

Keywords

Combination therapy, network rewiring, signal transduction, mechanistic modelling, in silico simulation.

Introduction

Aberrant signalling by specific members of the FGFR family, comprising FGFR1-4, occurs in a variety of human cancers, and can reflect FGFR gene mutation, fusion, amplification and/or overexpression, and also altered ligand expression (1). This has led to the development of selective small molecule drugs targeting these receptors, including Erdafitinib (an inhibitor of FGFR1-4), which was recently FDA-approved for patients with metastatic urothelial carcinoma exhibiting FGFR2/3 gene alterations and resistance to chemotherapy (2). While initial interest focused on FGFR1-3, oncogenic roles for FGFR4 in a variety of cancers have now become evident (3). In breast cancer, enhanced FGFR4 expression and mutation is associated with metastatic progression, particularly in the lobular subtype (4), and high FGFR4 expression positively correlates with endocrine resistance (4, 5). FGFR4 also drives phenotypic switching of luminal A breast cancers to a HER2-enriched gene expression phenotype (6), and is overexpressed in approximately one third of triple negative breast cancers (TNBCs) (7). A second cancer where FGFR4 is strongly implicated is hepatocellular carcinoma (HCC). Here, FGFR4 is activated as a consequence of overexpression of its ligand, FGF19, which is a 'driver' oncogene on the chromosome 11q13.3 amplicon (8). Reflecting this mechanism, FGF19 represents a predictive biomarker for response to anti-FGFR4 therapy across HCC cell lines and patient-derived xenografts (9). The accumulated evidence supporting oncogenic roles for FGFR4 has led to the development of BLU9931, BLU-554 (fisogatinib) and H3B-6527, small molecule drugs that selectively target and irreversibly bind this receptor. These drugs all exhibit promising pre-clinical activity in FGF19-driven HCC (9-11) and both fisogatinib and H3B-6527 are currently under evaluation in clinical trials for HCC patients with advanced HCC (NCT04194801 and NCT02834780).

While targeted therapies directed towards specific oncogenic protein kinases have greatly improved clinical management of particular cancers (12), intrinsic and acquired drug resistance remain a major problem. Well-established mechanisms that contribute to these resistance phenotypes include mutation of the target or downstream signalling proteins such as Ras, or the presence of by-pass signalling pathways (13). However, an additional mechanism that can limit the efficacy of targeted therapy is dynamic, adaptive rewiring of the cellular signalling network in response to treatment (1). For example, use of mTOR inhibitors can lead to enhanced PI3K/AKT signalling due to relief of negative feedback regulation of IRS-1 by S6K1, which lies downstream of mTORC1 (14). In addition, treatment with AKT or MEK inhibitors can lead to increased expression and/or activation of a suite of receptor tyrosine kinases (RTKs) that dampens the cellular response to the drug (15, 16). Importantly, characterization of network adaptation in response to drug treatment can inform the rational design of combination therapies that exhibit improved efficacy. For example, since kinome remodelling in response to AKT inhibition involves enhanced expression and activation of ErbB3, co-targeting of AKT and ErbB kinases achieves greater efficacy than either monotherapy (15).

Despite these advances, the complexity of kinase signalling networks presents a major roadblock to understanding mechanisms of adaptive resistance to targeted therapy (1). This complexity reflects the presence of features such as pathway crosstalk and both positive and negative feedback loops, and results in non-intuitive behaviour that makes logical prediction of signalling and biological outputs challenging. A powerful approach to address this issue is to integrate mathematical network modelling with experimental analysis in order to generate and validate predictive models. This can provide fundamental insights into the wiring of signalling networks and how this generates specific signalling behaviours and biological outputs. For example, application of this approach revealed the network basis for discriminating distinct ERK activity dynamics (17) and identified the incoherent feed-forward loop as a design principle underpinning network regulation of cell fate switching (18). In addition, it can be exploited to identify novel therapeutic strategies, as exemplified by accurate prediction of synergistic drug combinations stemming from establishment of a quantitative mechanistic model of the EGFR-PYK2-MET signalling network in triple negative breast cancer (19).

In this study, we developed a detailed mechanistic model of the FGFR4 signalling network and applied an integrative approach combining computational modelling and experimental studies to interrogate the dynamic rewiring of this network to anti-FGFR4 inhibition in cancer cells and identify combinatorial approaches that prevent or circumvent drug resistance. In addition, our work established new general quantitative metrics that characterise drug-induced rebound behaviours, and by generating cell type specific models through incorporation of protein expression data from hundreds of different cancer cell types, we demonstrate a remarkable diversity and heterogeneity in the signalling responses to FGFR4 inhibition across various and distinct cellular contexts. Overall, our work establishes an integrative framework for the network-level analysis of drug-induced signalling adaptation that can be applied not only to FGFR4 inhibition but also other kinase-directed targeted therapies.

Materials and Methods

Cell lines, cell culture and reagents

The TNBC cell line, MDA-MB-453 and HCC cell line, Hep3B were purchased from ATCC. MDA-MB-453 was cultured in RPMI-1640 (Gibco) supplemented with 10% (v/v) FBS (Moregate), 10 µg/mL Actrapid penfill insulin (Clifford Hallam Healthcare) and 20 mM HEPES (Gibco). Hep3B was cultured in EMEM (USbio) supplemented with 10% (v/v) FBS and 1 mM sodium pyruvate (Gibco). To passage cells, cells were washed once with 1x PBS, then detached from plates with 0.05% (w/v) trypsin/EDTA (Gibco) at 37°C in a 5% CO2 atmosphere. Trypsin was then inhibited with complete media.

For harvesting, cells at 80% confluency were washed twice with ice cold 1x PBS then lysed with RIPA buffer (0.5% (w/v) sodium deoxycholate, 150 mM NaCl, 1% (v/v) NP40, 50 mM Tris-HCl pH 8.0, 0.1% (w/v) SDS, 10% (v/v) glycerol, 5 mM EDTA and 20 mM NaF), supplemented with

10 µg/mL aprotinin, 1 mM PMSF, 10 µg/mL leupeptin, 1 mM sodium orthovanadate, 2.5 mM sodium pyrophosphate and 2.5 mM β-glycerophosphate prior to use. Lysed cells were collected and clarified by centrifugation at 21130 x *g* at 4°C for 10 min, then the protein concentration was determined using a Pierce BCA protein assay kit (Thermoscientific) according to the manufacturer's protocol.

Inhibitors and treatment

The following inhibitors were purchased from Selleckchem: FGFR4 inhibitor BLU9931 and H3B-6527, ErbB family inhibitor Lapatinib, PI3Kα inhibitor BYL719, pan-PI3K inhibitor BKM120, AKT inhibitor MK2206 and MEK inhibitor Trametinib. All inhibitors were reconstituted in DMSO.

For inhibitor treatment, cells were seeded into culture plates with an 80% end point confluence for all cell lines. After 24 h, cells were treated for the indicated times with the specific inhibitor or DMSO as vehicle control.

Generation of FGFR4 inhibitor resistant cells

MDA-MB-453 cells were seeded into 10 cm plates at a density of 500 cells. After 48 h, cells were treated with DMSO (as vehicle control) or FGFR4 inhibitor BLU9931 for at least 3 months. Culture medium was replaced twice a week. When cells formed colonies visible to the naked eye, small pieces of sterile filter paper soaked in trypsin were used to detach cells which were collected for further maintenance in media containing DMSO or FGFR4 inhibitor. These cells were termed long-term BLU9931 MDA-MB-453 cells in this study.

Immunoblotting

Protein lysates (25-40 µg) were prepared in 5x sample loading buffer (9% (v/v) glycerol, 0.03 M Tris/HCl pH 6.8, 2% (w/v) SDS, 0.05% (v/v) β-mercaptoethanol and 0.002% (w/v) bromophenol blue) and boiled for 10 min at 96°C. Western blot analysis was performed using SDS-PAGE on 4% (v/v) stacking gels and 8% (v/v) separating gels. Subsequently, resolved proteins were wet transferred onto PVDF membrane for 1 h, then blocked in 5% (w/v) BSA-TBS (50 mM Tris pH 7.5, 150 mM NaCl) blocking buffer for 1 h at RT, followed by incubation in primary antibody diluted in 5% (w/v) BSA/TBS with rolling overnight at 4°C. Following primary incubation, membranes were washed thrice with TBS-T (50 mM Tris pH 7.5, 150 mM NaCl, 0.1% (v/v) Tween 20) for 10 min, then probed with secondary antibody for 1 h at RT. Membranes were washed thrice again with TBS-T for 10 min before signal detection by ECL (Perkin Elmer) or Luminata Forte Western HRP substrate (Millipore) and images acquired with the ChemiDoc Touch Imaging system (Bio-Rad). Densitometry analysis was performed on the detected bands using ImageLab, version 5.2.1 (Bio-Rad). β-actin or α-tubulin were used as the loading controls. The intensity of each band was normalised against the intensity of their corresponding loading control. Bands corresponding to phospho-proteins were further normalised to the bands of corresponding total protein levels.

The following antibodies were purchased from Cell Signaling Technology: pan-phosFGFR (Y653/654) (3471), AKT (4685), ERK (4695), pAKT (S473) (4058), pERK (T202, Y204) (4370), pFRS2 (Y436) (3861), ALK (3333), pALK (Y1096) (4143), pALK (Y1282/1283) (9687), pALK (Y1078) (4144), ErbB2 (2165), pErbB2 (Y1248) (2247), ErbB3 (4754), pErbB3 (Y1328) (8017), IGF-1R (9750) and GSK (5676). The following antibodies were purchased from Santa Cruz Biotechnology: FGFR4 (sc-136988) and β-actin (sc-69879). The α-tubulin (T5168) and FRS2 (05-502) antibodies were purchased from Sigma-Aldrich. The pIRS-1 (Y612) (44-816G) and pIGF-1R (Y1162/1163) (44-804G) were purchased from Biosource. An IRS-1 (6248) antibody was purchased from Upstate and a pGSK (Y216/279) (ab4797-50) was purchased from Abcam.

Cell viability assays

Cell viability determined by direct cell counting was performed by seeding cells into 6 well plates and culturing for 7 days. Cells were washed with 1x PBS then trypsinised at 37°C in a 5% CO2 atmosphere until detachment. Trypsinised cells were then resuspended thoroughly in complete media to inhibit trypsin. Cells were stained with Trypan blue (EVS-1000, NanoTek), then transferred to an EVE cell counting slide (EVS-1000, NanoTek) and counted with the EVE automatic cell counter (EVE-MC-DEMO, NanoTek) according to the manufacturer's protocol.
For MTS proliferation assays, 3000 cells were seeded into 96 well plates and cultured for the indicated days. Cell viability was determined using the CellTiter 96 Aqueous One Solution Cell Proliferation Assay (Promega) according to the manufacturer's protocol. 20 µL of reagent was added into the wells and incubated at 37°C in a 5% CO2 atmosphere for 45 mins. Absorbance was determined using the PHERAstar microplate reader (BMG LABTECH).

RNA isolation, RT-PCR and Sanger sequencing

Total RNA was isolated from parental MDA-MB-453 and long-term BLU9931 MDA-MB-453 cells using a RNeasy mini kit (Qiagen) following the manufacturer's protocol. RNA was quantified using a Nanodrop ND-1000 (NanoDrop Technologies). RNAs were reverse transcribed using a high-capacity cDNA reverse transcription kit (Thermoscientific). Subsequently, cDNA was amplified by PCR to identify gatekeeper mutations in the FGFR4 kinase domain using forward (F) primers and reverse (R) primers (Table S4). The PCR products were resolved by gel electrophoresis, and the bands at the predicted product size were excised and purified with a gel and PCR clean-up system (Promega). Sanger sequencing was completed by the Micromon facility at Monash University. Reactions were repeated on three biological replicates.

Statistical analysis

Quantification of western blots by densitometry was performed using ImageLab version 5.2.1 (Bio-Rad) and statistical t-tests were performed using GraphPad Prism 8 and Microsoft-Excel.

Computational modelling

The FGFR4-centered model was formulated using ordinary differential equations (ODEs). The rate equations and full set of ODEs are given in Supplementary Tables S1-2. The model construction and calibration processes were implemented in MATLAB (The MathWorks. Inc. 2019a) and the IQM toolbox (http://www.intiquan.com/intiquan-tools/) was used to compile the IQM file for a MEX file which makes the simulation faster. To facilitate model exchange, an exchangeable Systems Biology Markup Language (SBML) file of the model is provided as Supplementary File 1. The code for the modelling has been deposited to Github and can be accessed at https://github.com/NguyenLab-IntegratedNetworkModeling/FGFR4_model.

Model calibration

The adequacy and specificity of a mathematical model is generally justified by its ability to recapitulate experimental data. This is achieved through model calibration (also referred to as model training or fitting) that involves estimation of the unmeasured model parameters so that simulations using these parameter values (called best-fitted parameter sets) could recapitulate the training data. Here, parameter estimation was done by minimizing an objective function J that quantifies the discrepancies between model simulations and the corresponding experimental measurements. A genetic algorithm was used to optimize the objective function (20-22), utilising the Global Optimization Toolbox and the function *ga* in MATLAB. Model calibration was carried out on a virtual machine consisting of 32 Intel Xeon 2.10 GHz processors running in parallel. A more detailed description of the model calibration process is given in Supplementary Text S1. As a result, we obtained 5 best-fitted parameter sets that were collectively used for model simulations; these are given in Supplementary Table S3.

Model-based computation of drug synergy

Using our network model, we evaluated *in silico* the efficacy and possible synergism of 20 possible combinatorial strategies co-targeting FGFR4 and each of 20 network components. Drug synergy was computed based on the coefficient of drug interaction (CDI) metric (23, 24): $CDI=E_{12}/(E_1 \times E_2)$, where E_{12} is a normalized biological response (e.g., cell viability) by the combined treatment of drug 1 and 2, and E_1 and E_2 are the response by the single drug treatment, respectively. CDI <1, = 1 or >1 indicates that the drugs are synergistic, additive or antagonistic, respectively.

To comparatively assess the effect of the single-drug and combination treatments, we introduced a theoretical cell viability (ICV) function, defined as the aggregate of the activated levels of the major pro-growth signalling nodes in the model: $ICV = [pIGFR] + [pFGFR4] + [pERBB] + [pAKT] + [aRas] + [pERK]$. For each treatment, the corresponding ICV value could be computed using the model. Computationally, a treatment that results in a lower ICV value is assumed to be more effective in suppressing cell viability.

RESULTS

FGFR4 inhibition rewires signalling networks in MDA-MB-453 cells leading to upregulation of AKT activity

To determine the effects of the selective and irreversible FGFR4 inhibitor BLU9931 on FGFR4 downstream signalling and cell proliferation in TNBC, the MDA-MB-453 cell line that exhibits an activating mutation in FGFR4 (25) was utilised. The MDA-MB-468 cell line with no detected FGFRs was used as a negative control (26). MDA-MB-453 cells were treated with different concentrations of BLU9931 for 1 h. Total FGFR4 expression was not affected by BLU9931, but the treatment decreased pFGFR at concentrations of 3nM and higher (Fig. 1A), and this effect was paralleled by a significant decrease in downstream signalling proteins pFRS2, pERK and pAKT (Fig. 1A, B). BLU9931 also significantly decreased cell proliferation of MDA-MB-453 cells at 10nM from day 3 onwards but did not affect MDA-MB-468 cells (Fig. 1C).

To understand how FGFR4 inhibition temporally influences downstream signalling, MDA-MB-453 cells were treated with 10nM of BLU9931 for 1, 4, 8 and 24 h (Fig. 1D). The levels of pFRS2 and pERK were initially decreased, followed by some signal recovery at 24 h (Fig. 1D). However, pAKT levels decreased after 1 h of drug treatment but the signal recovered at 4 h and then increased at 8 h and 24 h relative to the vehicle control (Fig. 1D). This suggests that the FGFR4 signalling network is being dynamically rewired following the inhibitor treatment. To identify if the 'bounce-back' of pAKT is independent of the inhibitor used, MDA-MB-453 cells were treated with another FGFR4 inhibitor, H3B-6527 and this resulted in the same pAKT 'bounce-back' effect at the same time points (Fig. S1A). This suggests a general rewiring phenomenon following FGFR4 inhibition in MDA-MB-453 cells.

A computational mechanistic model of the FGFR4-centred signalling network

The unexpected and marked rebound of pAKT in MDA-MB-453 cells after BLU9931 and H3B-6527 treatment suggests pathway rewiring to compensate the FGFR4 inhibition. Given the complexity of the signalling network surrounding FGFR4, we developed a detailed computational model to achieve a systems-level understanding of the potential compensatory mechanisms in this system. Our model included the major effectors and pro-growth signalling pathways downstream of FGFR4, such as the FRS2, PI3K/AKT/mTOR and Ras/RAF/MEK/ERK signalling pathways. A simplified model scheme is displayed in Fig 2A and the model's detailed reaction map is provided in Fig S2. Since these pathways are also converged upon by other RTKs, the model also incorporated the RTKs of the IGFR/IR and ErbB receptor families. As feedback loops and crosstalk are critical in shaping signalling drug response (30-32), the model (hereafter the 'FGFR4 model') accounted for previously described feedback and crosstalk mechanisms within the integrated FGFR4 network (Fig 2A). The new model was formulated using ordinary differential equations (ODEs) and implemented in MATLAB that mathematically represents the network

interactions based on established kinetic laws (see Materials and Methods and Table S1-2 for detailed model descriptions).

To provide our model with context specificity and predictive capability, we calibrated (trained) it against experimental data using a combination of drug-treated time-course and dose-response signalling data from the MDA-MB-453 cells, as measured by Western blot in Fig. 1A-B,D, and S1B. Model training involved the estimation of unknown model parameters using a genetic algorithm (GA)-based optimisation procedure so that model simulations recapitulated the experimental data (see Materials and Methods). As a result, we obtained five best-fitted parameter sets that were collectively used for further analysis in order to avoid possible biases associated with any single sets (best-fitted parameter values are given in Table S3). Model simulations using the best-fitted sets demonstrated good concordance with the quantified experimental data (Fig. 2B), suggesting the calibrated model could qualitatively and quantitatively reproduce the data.

Co-targeting of FGFR4 and AKT, but not PI3K, eliminates pAKT rebound and suppresses MDA-MB-453 cell proliferation

To determine if the rebound in AKT signals upon treatment with FGFR inhibitors is dependent on the drug dosage, we simulated the temporal response of pAKT to increasing doses of BLU9931 using the calibrated model. Interestingly, the model predicted that at a higher dose (10nM), BLU9931 induced an even stronger rebound in pAKT compared to the lower dose (3nM), that was more pronounced at the later time points (Fig. 3A). Given PI3K is a direct upstream kinase of AKT signalling, we asked if co-targeting FGFR4 with PI3K may eliminate the pAKT rebound. *In silico* model simulations showed that while the combined FGFR and PI3K inhibition (PI3Ki) significantly suppressed pAKT levels at both the early and late time points, the combinatorial treatments did not completely abolish the rebound pattern of pAKT (Fig. 3B,C), which recovered to almost pre-treated levels with the high dose of BLU9931 + PI3Ki (Fig. 3D).

To experimentally validate these model predictions, we treated MDA-MB-453 cells with the PI3K-α inhibitor BYL719 and pan-PI3K inhibitor BKM120 for 1 h at varying concentrations (Fig. S3A,B). These results allowed selection of specific concentrations of each inhibitor to use in combination with BLU9931. Then, MDA-MB-453 cells were treated with BLU9931, BYL719 or BKM120 alone or combinations of BLU9931 with either PI3K inhibitor for 1 and 24 h (Fig. 3E). The highest dose of BLU9931, BYL719 and BKM120 decreased pAKT at 1 h, as did all the combination treatments (Fig. 3E,F). Consistent with model prediction, the higher dose of BLU9931 triggered a stronger rebound of pAKT at 24 h, particularly in the presence of BYL719 (Fig 3E,F). Furthermore, while the BLU9931+BYL719 combination treatments better suppressed the pAKT signal recovery relatively to BLU9931 alone, the combined treatments did not completely eliminate the rebound, as predicted by our model (Fig.3F). This failure to eliminate rebound was similarly observed for the BLU9931+ BKM120 combination (Fig. S4). Next, to determine whether pAKT signal dynamics predict the cellular growth response, we measured cell

proliferation in response to the single and combination treatments of BLU9931 and BYL719 or BKM120. Administration of BLU9931, BYL719 or BKM120 significantly decreased proliferation of MDA-MB-453 cells (Fig. 3G,H). However, combining BLU9931 with BYL719 (or BKM120) exhibited a similar effect to single inhibitor treatment (Fig. 3G,H), consistent with effects on AKT activation.

Next, we simulated the combined effect of BLU9931 and AKT inhibition (AKTi) on pAKT. Unlike PI3Ki, model simulations predicted a complete elimination of BLU9931-induced pAKT rebound by the co-administration of AKTi (Fig. 3I). To confirm this experimentally, we treated MDA-MB-453 cells with BLU9931 and the AKT inhibitor MK2206 alone or in combination (Fig. 3J&S5) for 4 h and 24 h. Treatment with the BLU9931+MK2206 combination potently suppressed pAKT at 24 h, consistent with our model prediction (Fig. 3I-J). Individual treatment with MK2206 also suppressed pAKT to a greater extent than BLU9931 alone at 4 h (Fig. 3J). This marked suppression of pAKT with MK2206 is expected because AKT is inhibited directly, unlike the situation with PI3K inhibitors, which inhibit PI3K upstream of AKT. Consistent with these data, treatment with MK2206 significantly decreased proliferation of MDA-MB-453 cells (Fig. 3K). Moreover, combining BLU9931 with MK2206 was significantly more effective in blocking cell proliferation than either agent alone (Fig. 3K).

Collectively, our results indicate that the efficacy of BLU9931 is limited by the 'bounce-back' of AKT which can be blocked by an AKT inhibitor but not PI3K inhibitors. The combination of BLU9931 with MK2206 is more effective than individual treatments in inhibiting cell proliferation because the former drug suppresses other signalling pathways (e.g. ERK), while the latter inhibits AKT, leading to an overall suppression of downstream signalling.

Upregulated RTKs in parental and BLU9931-resistant MDA-MB-453 cells

While FGFR4 inhibition results in dynamic reactivation of AKT, the network rewiring mechanism that underpins this remains unclear. Since such signalling bounce-back is often caused by loss of negative feedback signals to upstream network nodes including specific RTKs (30-32), we asked if this was the case in our system. To explore this, we extended our model simulation readouts beyond pAKT and simulated the response of pIGF1R, pIRS and pErbBs to BLU9931 in a time- and dose-dependent manner (Fig. 4A and Fig S6), as these proteins are under regulation of multiple negative feedback loops (Fig. 2A). Time-course simulations predicted a strong and significant upregulation of pIGF1R, pIRS and pErbB at 24 h following BLU9931 treatment, both at low (10nM) and high (100nM) doses (Fig. 4A). Moreover, the dose-dependent simulations suggested that higher BLU9931 concentrations led to stronger upregulation of these proteins (Fig S6), as seen previously for pAKT (Figs. 3A-D). These model predictions led us to hypothesize that FGFR4 inhibition remodelled the RTK network in TNBC cells, which caused pAKT rebound and compromised the inhibitory effect of BLU9931 on cell proliferation.

To test this hypothesis and the model predictions, we first characterized the temporal expression and phosphorylation of particular RTKs in MDA-MB-453 cells after 1 h and 24 h BLU9931 treatment. In agreement with model predictions, we observed a marked upregulation of pIGF1R, pIRS and pErbB2-3 at 24 h compared to the vehicle control or 1 h treatment (Fig. 4B), and as predicted, these upregulations were more pronounced at the higher concentration of BLU9931 (100nM vs. 10nM, Fig. 4B).

In addition to investigating the short-term remodelling of the FGFR4 network in response to BLU9931, we also interrogated the long-term effects of treatment with this drug. To this end, MDA-MB-453 cells were exposed to BLU9931 for at least 3 months until visible colonies formed, allowing isolation of resistant cells (see Material and Methods). Compared to parental cells, long-term drug-treated cells were not significantly growth-inhibited by 10 nM BLU9931, and the effect of 100 nM drug treatment was markedly reduced (Fig. 4C,D).

Since FGFR4 kinase domain gatekeeper mutations are an important mechanism for development of resistance to anti-FGFR4 small molecule drugs (27), we first subjected the FGFR4 kinase domain in parental and long-term BLU9931 cells to DNA sequencing. However, FGFR4 gatekeeper mutations were not detected (Fig S7). Next, we characterized the expression profile of FGFR4 signalling network components. Interestingly, similar to parental cells treated with BLU9931 for 24 h, long-term BLU9931-treated cells demonstrated a marked upregulation of pAKT, pIGF1R, pIRS and pErbB2-3 (Fig. 4B). Of note, levels of phosphorylated GSK3α/β and pY1248 ErbB2 were higher in the long-term BLU9931-treated cells than in parental cells treated for 24 h with BLU9931 (Fig. 4B). Consequently, while increased activation of particular RTKs induced by 24 h BLU9931 treatment is maintained in the long-term drug-refractory cells, additional changes occur that likely underpin the long-term resistance to BLU9931. These integrative data highlight upregulated RTKs and other signalling nodes that represent potential targets for combination treatments with BLU9931, a concept that is formally addressed in the following section.

Model prediction and validation of synergistic drug combinations co-targeting FGFR4

While complex interactions within the FGFR4 network pose significant challenges to the identification of effective drug combinations (32, 33), our computational model provides a powerful framework for the systematic prediction of nodes that could be targeted along with FGFR4 to overcome adaptive resistance to anti-FGFR4 monotherapy. To explore this, we simulated *in silico* the efficacy of 20 possible pair-wise drug combinations co-targeting FGFR4 and each of 20 other network nodes using our model (Fig. 5A). The performance of each combination was theoretically evaluated by computing a coefficient of drug interaction (CDI, see Materials and Methods for details) that quantifies how well it suppresses cell proliferation in comparison to the single-drug treatments (Fig. 5A). CDI <1, =1, >1 indicates synergistic, additive or antagonistic effects, respectively; and its value signifies the magnitude of

synergism/antagonism. Sorting the CDI scores allowed us to rank and prioritise the drug combinations according to their predicted synergistic effects (Fig. 5A).

The model predicted that combined inhibition of FGFR4 and the ErbB receptors represented the most synergistic combination, followed by co-inhibition of FGFR4 and AKT, PDK1 or IGF1R (Fig. 5A). In contrast, co-targeting FGFR4 and PI3K or FGFR4 and MEK/SHP2 was predicted to be not synergistic. The fact that the model correctly predicted the synergistic effect of co-targeting FGFR4 and AKT, but not PI3K (Fig. 3), lends support to the validity of our approach. In addition, the presence of ErbBs and IGF1R amongst the top predicted synergistic co-targets is consistent with our data demonstrating upregulation of these RTKs in response to acute FGFR4 inhibition and in the long-term resistant cells (Fig. 4).

Since ErbBs were predicted to be the most synergistic FGFR4 co-target, we next aimed to validate this prediction. To suppress the activity of ErbB2, the long-term BLU9931-maintained cells were treated with Lapatinib, with 100 nM selected as the most appropriate dose (Fig. 5B,C). Lapatinib treatment alone had no effect on either parental or resistant cells (Fig. 5D-G). In cells maintained long-term in 10 nM BLU9931, the combination treatment with Lapatinib restored growth inhibition (Fig. 5F). At 100 nM BLU9931, the combination treatment caused cell death in both parental (Fig. 5E) and resistant cells (Fig. 5G). These results indicate that although the parental cells exhibit similar RTKs upregulated 24 h post-BLU9931 treatment, the long-term BLU9931-maintained cells may be more dependent on ErbB2, consistent with the presence of enhanced Y1248 phosphorylation. Taken together, our computational analyses and experimental validation demonstrate that co-targeting ErbB2 can synergistically enhance the efficacy of FGFR4 inhibition in MDA-MB-453 TNBC cells.

Model-based identification of network connections underpinning pAKT rebound

Our results so far implicate the upregulation of RTKs such as particular ErbBs and IGF1R in the reactivation of pAKT after FGFR4 inhibition, yet the precise network interactions that mediate the pAKT rebound remain unclear. In this section, we leveraged the mechanistic nature of our model to computationally interrogate which regulatory links are essential in mediating pAKT's rebound pattern. First, we performed model sensitivity analysis where we systematically blocked the network links by inhibiting the corresponding kinetic parameter values one at a time by 75%, and simulated the resulting pAKT time-course following BLU9931 treatment (Fig. 6A). Visual inspection indicated significant changes to the pAKT dynamics, which were highly specific to the perturbed parameters (Fig. 6A). To assess these changes quantitatively, we defined two general metrics characterising a typical drug-induced rebound dynamic pattern: (i) a *'rebound'* (RB) and an *'early drug effect'* (EDE), deriving from 3 basic measures: B = the pre-treated level, C = the minimal level, and the rebound steady-state level (Y), as shown in Fig. 6B. Accordingly, a higher RB score reflects a more dramatic rebound and a higher EDE score means the drug effect is more potent initially. We then applied these scores to the sensitivity analysis of kinetic parameters controlling the pAKT rebound dynamics (Fig. 6C). We found that for > one-third of the model

parameters, blocking them significantly decreased the RB score, suggesting a positive role for these links in mediating pAKT rebound (Fig. 6C). In contrast, almost a half of the remaining parameters had the opposite effect, while the other half did not significantly influence the RB score (Fig. 6C). Interestingly, there was generally an inverse correlation between the RB and EDE scores (Fig. 6C and S8), indicating that parameters that increased pAKT rebound also tended to decrease the initial drug effect on pAKT, as seen visually in Fig. 6A.

Next, to provide greater insights into the parameter effects on the RB and EDE scores, we performed a clustering analysis of these scores and classified the parameters into two distinct groups with opposing effects on pAKT response (Fig. 6D). Blocking the parameters in group A led to reduced pAKT rebound (also a lower steady state) and enhanced the early inhibitory effect of the drug on pAKT (Fig. 6E, blue curves); while blocking those in group B potentiated pAKT rebound and also blunted the initial drug effect on pAKT (Fig. 6E, red curves). Mapping these parameters onto the network schematic diagram highlighted specific network interactions, including feedback loops and cross-pathway connections that modulate the pAKT response in opposite fashions (Fig. 6F).

Diverse pAKT/pERK response profiles following FGFR4 inhibition across cancer cell lines

Previously, we determined that cell-to-cell variation in protein expression levels is a major source of signalling response heterogeneity (28). This led us to hypothesize that FGFR4 inhibitor-induced signalling dynamics may be dictated by the protein expression profile across specific cancer cell types. To address this hypothesis, we obtained protein expression data for 350 different cancer cell lines of diverse tissue origins from the Cancer Cell Line Encyclopaedia (CCLE) consortium (35), and used these as inputs to customize our MDA-MB-453 model, generating 350 models that reflect the specific protein expression profile of each cell type (see Fig S9A for detailed workflow). Using these cell type-specific models, we simulated the temporal profiles of pAKT and pERK in response to FGFR4 inhibition in each cell type. Hierarchical clustering analysis revealed a remarkable heterogeneity in the response of these outputs, ranging from no significant change to strong rebound to straight increase patterns for pAKT (Fig. 7A), while pERK predominantly displayed rebound or monotonic decrease patterns (Fig. 7B). By defining 3 types of possible composite patterns: REB (rebound), INC/NOC (increase/no significant change) or DEC (decrease), we further classified the cell lines into subgroups with distinct response profiles of pAKT-pERK, resulting in 4 major subgroups: REB-REB (Group 1), INC/NOC-REB (Group 2), REB-DEC (Group 3) and INC/NOC-DEC (Group 4) (Fig. 7C and Fig. S9B). Interestingly, FGFR4i induced pERK rebound in about one-third of the cell lines (34%), indicating that re-activation of ERK represents a salient response feature post FGFR4i treatment in a subset of cell types that likely blunts the treatment effect. In addition, while pAKT displayed rebound in about 9% of the cell lines, our simulations suggest that in the remaining cell lines (91%) FGFR4i either did not significantly affect or even induced a straight increase of pAKT, indicating bounce-back may not be the only dynamic feature underpinning the ability of AKT to mediate FGFR4i resistance. In

particular, nearly two-third (63%) of the cell lines displayed concomitant pAKT increase/no change and pERK decrease, and 7% exhibited rebound in both pAKT and pERK (Fig. 7C).

We next asked whether it is possible to switch from one group to another by modulating particular network components. To address this, we utilised the MDA-MB-453 model (representing Group 1), and systematically perturbed the expression levels of every network component, in order to determine whether we could convert the pAKT response from REB to INC (Group 1 → Group 2) or pERK response from REB to DEC (Group 1 → Group 3). This perturbation analysis showed that either downregulation of FGFR4, FRS2, Grb2 or Ras, or upregulation of CBL, IGF1R, IRS or PI3K switched pAKT from rebound to increase (Fig. 7D and Fig. S10); while downregulation of ERK, MEK, Raf, Ras or upregulation of AKT switched pERK from rebound to decrease (Fig. 7E and Fig. S10). Overall, these findings highlight the remarkable plasticity of signalling networks and the need to embrace network context in the analysis of drug-induced network remodelling.

Alternative network rewiring following selective FGFR4 inhibition in Hep3B cells

Our model-based analysis above predicted different subgroups of cancer cell types with contrasting response patterns for pAKT-pERK that likely compromise the effect of FGFR4 inhibition. Group 1 is exemplified by the MDA-MB-453 cell line (Fig. 1D). To further test the model prediction and the validity of Group 2, we identified the HCC cell line Hep3B to be a member of this group (Fig. S11A). Hep3B displays active FGFR4 signalling due to gene amplification of the FGFR4 ligand, FGF19 (9).

To investigate the network rewiring mechanisms following anti-FGFR4 treatment in Hep3B, we exposed these cells to H3B-6527 (9). Cells treated with this drug at concentrations of 5nM or higher demonstrated a marked decrease in pFRS2 and pERK after 1 h (Fig. S11B). Consistent with our prediction for the behaviour of Group 2, cells treated with H3B-6527 demonstrated an early and temporally increasing rebound of pERK levels despite the on-target drug effect evident by the durable suppression of pFRS2 (Fig. 7F and S11B). In addition, pAKT displayed no significant change following H3B-6527 treatment in Hep3B (Fig. S11B, C), which is also in accordance with Group 2 behaviour. These dynamic responses are in contrast to the patterns observed in MDA-MB-453, where strong pAKT rebound is a salient property and early pERK rebound is absent. Together, these data confirm the validity of group 2 and validate Hep3B as an example member of this group.

The rebound recovery of pERK signals after H3B-6527 treatment suggested that co-targeting ERK may restore the sensitivity of Hep3B cells to H3B-6527. To test this, we first determined the appropriate concentration of Trametinib, a MEK inhibitor that targets the MAPK signalling pathway upstream of ERK, for combination treatments. Trametinib at 5nM or higher decreased pERK in Hep3B cells (Fig. S11D). Next, Hep3B cells were treated with H3B-6527 and Trametinib, alone or in combination. While both H3B-6527 and Trametinib alone both

significantly decreased Hep3B cell proliferation (Fig. 7G-H), the combination treatment resulted in a significantly greater effect (Fig. 7H). This indicates that the efficacy of H3B-6527 is improved by blocking the ERK 'bounce-back' and highlights this combination treatment as a promising therapeutic approach for HCC.

Discussion

Tumour cells evade targeted cancer therapies via an elaborate repertoire of resistance mechanisms. One common theme involves rapid and dynamic rewiring of signalling pathways in order to bypass the drug blockade (15, 16, 29-31). Network adaptation occurs across different cancer types in preclinical models (16, 32, 33) as well as in patients (34), highlighting adaptive resistance as a major challenge to the clinical success of cancer therapies. However, pathway crosstalk and feedback render signalling responses to targeted treatment highly non-linear (35, 36), making it difficult to predict their behaviour. An in-depth understanding of adaptive resistance requires an ability to integrate signalling pathways in unified predictive frameworks and to describe their dynamics quantitatively at a system level. In this study, we developed a detailed ODE-based dynamic model of the FGFR4 signalling network that incorporates major cell-surface receptors and key convergent signalling pathways. Rigorous model calibration and validation using time-resolved drug perturbation data from MDA-MB-453 TNBC cells allowed the model to be specifically tailored to this cell type and ensured its validity. To our knowledge, this represents the first instance of a detailed and experimentally-validated model of the FGFR signalling network. In addition, we utilized our systems-based approach to characterise adaptive resistance to anti-FGFR4 inhibition in FGFR4-driven cancers, and identified combinatorial strategies that overcome drug resistance.

Combining model simulation and experimental analysis, we demonstrated that in MDA-MB-453 cells, inhibition of FGFR4 by selective inhibitors led to a strong reactivation of the pro-survival protein AKT. As AKT signalling is critical for FGF19-FGFR4 mediated growth in breast cancer cells (37), this 'bounce-back' of AKT signal indicates that the FGFR4 network is dynamically rewired to overcome FGFR4 inhibition. These results further imply that a combination of FGFR4 and PI3K or AKT inhibitors may be a more effective therapeutic strategy than targeting FGFR4 alone. However, our model simulations predicted that co-targeting of FGFR4 and AKT, but not PI3K, would effectively eliminate the pAKT rebound. This was subsequently validated experimentally, where the combination of BLU9931 with an AKT inhibitor potently suppressed AKT activation rebound and cell proliferation. Consistent with these data, the selective FGFR1-3 inhibitor AZD4547 and AKT inhibitor AZD5363 exhibited additive effects against FGFR1-expressing prostate cancer *in vitro* and *in vivo* (38). Furthermore, since mTOR signals downstream of AKT, mTOR inhibitors may also be promising in combination therapy. In support of this, the mTOR inhibitor AZD2014 in combination with AZD4547 demonstrated

552 tumour growth attenuation in tumour xenografts generated from FGFR1-dependent lung cancer
553 cells (39).
554
555 Combinatorial targeting of FGFR4 is a relatively understudied area, and most work has focused
556 on combining FGFR4 inhibition with radio/chemotherapeutics (40, 41). In order to expedite
557 identification of novel combination treatments that target FGFR4 together with other RTKs and
558 signalling proteins, we exploited the mechanistic and quantitative nature of our model to predict
559 the effect of 20 possible pair-wise drug combinations co-targeting FGFR4 and other network
560 components in a systematic and unbiased manner. Among the different components, ErbB
561 receptors were predicted to be the most synergistic FGFR4 co-target. This was confirmed
562 experimentally, where combined inhibition of FGFR4 and ErbB2 using BLU9931 and Lapatinib,
563 but not administration of the individual drugs, resulted in death of both the parental and long-term
564 BLU9931-resistant cells. These findings are consistent with the activation of alternative RTKs as
565 an escape mechanism previously reported in FGFR-resistance models (42, 43). For example,
566 FGFR3-dependent bladder cancer cell lines developed resistance to the pan-FGFR inhibitor
567 BGJ398 by switching receptor signalling to ErbB2 or ErbB3, and here the dual inhibition of
568 FGFR3 and ErbB activity resulted in increased cell death (42). Also, unbiased screening using
569 pTyr RTK arrays identified high levels of pEGFR and pErbB2 in two FGFR-dependent basal-like
570 breast cancer tumour xenografts after FGFR inhibition (44), and combining the pan-ErbB inhibitor
571 AEE788 and multi-kinase pan-FGFR inhibitor Dovitinib resulted in inhibition of the downstream
572 FRS2-ERK and AKT pathways and tumour growth and metastasis (44).
573
574 Our model-based perturbation analysis also identified points of network interference that could
575 switch the response behaviour from one pattern to another, e.g. from a rebound in activation of
576 pAKT to a progressive increase, highlighting how the plasticity of signalling networks provides a
577 mechanism to modulate drug response. It is likely that cancer cells exploit this capability to switch
578 from a drug-sensitive to a drug-resistant state. On the flip side, a detailed understanding of network
579 behaviour and adaptability will aid the design of novel therapeutic strategies to counter drug-
580 induced re(activation) of pro-growth signalling, e.g. by converting (re)activation of pAKT/pERK
581 to a reduction in activity. Overall, these findings highlight integrative network modelling as a
582 powerful approach to analyse and predict network changes required for manipulating specific
583 signalling behaviours.
584
585 It has become increasingly appreciated that the mechanisms underpinning adaptive resistance
586 can be highly heterogeneous and context-specific, even in response to the same drug compounds
587 (45). This is primarily driven by variation in protein expression and/or mutational profiles
588 observed across and within different cancer cell types, resulting in context-specific differences in
589 feedback and crosstalk strengths that impact on drug response (19, 28). For example, BRAF
590 inhibition by vemurafenib is effective in BRAF-mutant melanoma but not colorectal cancer,
591 reflecting higher EGFR expression in the latter cancer type. Consequently, in colorectal cancer,

vemurafenib induces feedback activation of the EGFR that allows continued MAPK signalling and cellular proliferation (46). However, due to the complexity of signalling networks and lack of predictive models, our ability to predict context-dependent network rewiring remains limited. Here, we incorporated publicly available protein expression data from hundreds of cancer cell types to adjust the state variables of our model, enabling us to adapt the model to diverse cellular contexts and identify four major response patterns for pAKT and pERK. Amongst the cell types exhibiting increase/no change pattern in AKT activation in combination with ERK rebound, we identified and experimentally validated the HCC cell line Hep3B. Importantly, co-targeting FGFR4 and MEK (upstream of ERK) in Hep3B cells markedly enhanced inhibition of cell proliferation. Together, our results highlight co-targeting FGFR4 and ERK as a novel precision treatment strategy for HCC.

Overall, through an integrative approach we have identified mechanisms of FGFR4 pathway rewiring and identified potential combination targeted therapies with increased efficacy for FGFR4-driven TNBC and HCC cancers. Given that co-targeting FGFR4 and ErbB2 was particularly effective, there is significant potential in expanding this targeted treatment strategy to other breast cancer subtypes of poor prognosis, including luminal B and HER2 breast cancers. Finally, the computational models and integrative systems-based approach utilised provide a valuable foundation for future investigation of network rewiring and adaptive resistance related to targeting of other RTKs in breast cancer as well as other malignancies.

References

1. I. S. Babina, N. C. Turner, Advances and challenges in targeting FGFR signalling in cancer. *Nat Rev Cancer* **17**, 318-332 (2017).
2. Y. Loriot *et al.*, Erdafitinib in Locally Advanced or Metastatic Urothelial Carcinoma. *N Engl J Med* **381**, 338-348 (2019).
3. K. M. Levine, K. Ding, L. Chen, S. Oesterreich, FGFR4: A promising therapeutic target for breast cancer and other solid tumors. *Pharmacology & Therapeutics* **214**, 107590 (2020).
4. K. M. Levine *et al.*, FGFR4 overexpression and hotspot mutations in metastatic ER+ breast cancer are enriched in the lobular subtype. *npj Breast Cancer* **5**, 19 (2019).
5. D. Meijer *et al.*, Fibroblast growth factor receptor 4 predicts failure on tamoxifen therapy in patients with recurrent breast cancer. *Endocr Relat Cancer* **15**, 101-111 (2008).
6. S. Garcia-Recio *et al.*, FGFR4 regulates tumor subtype differentiation in luminal breast cancer and metastatic disease. *J Clin Invest* **130**, 4871-4887 (2020).

7. N. J. Chew *et al.*, Evaluation of FGFR targeting in breast cancer through interrogation of patient-derived models. *Breast Cancer Res* **23**, 82 (2021).
8. E. T. Sawey *et al.*, Identification of a therapeutic strategy targeting amplified FGF19 in liver cancer by Oncogenomic screening. *Cancer Cell* **19**, 347-358 (2011).
9. J. J. Joshi *et al.*, H3B-6527 Is a Potent and Selective Inhibitor of FGFR4 in FGF19-Driven Hepatocellular Carcinoma. *Cancer Res* **77**, 6999-7013 (2017).
10. M. Hagel *et al.*, First Selective Small Molecule Inhibitor of FGFR4 for the Treatment of Hepatocellular Carcinomas with an Activated FGFR4 Signaling Pathway. *Cancer Discov* **5**, 424-437 (2015).
11. R. D. Kim *et al.*, First-in-Human Phase I Study of Fisogatinib (BLU-554) Validates Aberrant FGF19 Signaling as a Driver Event in Hepatocellular Carcinoma. *Cancer Discovery* **9**, 1696-1707 (2019).
12. E. D. Fleuren, L. Zhang, J. Wu, R. J. Daly, The kinome 'at large' in cancer. *Nat Rev Cancer* **16**, 83-98 (2016).
13. P. Saraon *et al.*, Receptor tyrosine kinases and cancer: oncogenic mechanisms and therapeutic approaches. *Oncogene* **40**, 4079-4093 (2021).
14. K. E. O'Reilly *et al.*, mTOR Inhibition Induces Upstream Receptor Tyrosine Kinase Signaling and Activates Akt. *Cancer Research* **66**, 1500-1508 (2006).
15. S. Chandarlapaty *et al.*, AKT inhibition relieves feedback suppression of receptor tyrosine kinase expression and activity. *Cancer Cell* **19**, 58-71 (2011).
16. J. S. Duncan *et al.*, Dynamic reprogramming of the kinome in response to targeted MEK inhibition in triple-negative breast cancer. *Cell* **149**, 307-321 (2012).
17. T. Nakakuki *et al.*, Ligand-specific c-Fos expression emerges from the spatiotemporal control of ErbB network dynamics. *Cell* **141**, 884-896 (2010).
18. S. Y. Shin *et al.*, The switching role of beta-adrenergic receptor signalling in cell survival or death decision of cardiomyocytes. *Nat Commun* **5**, 5777 (2014).
19. S. Y. Shin, A. K. Muller, N. Verma, S. Lev, L. K. Nguyen, Systems modelling of the EGFR-PYK2-c-Met interaction network predicts and prioritizes synergistic drug combinations for triple-negative breast cancer. *PLoS Comput Biol* **14**, e1006192 (2018).
20. F. Reali, C. Priami, L. Marchetti, Optimization Algorithms for Computational Systems Biology. *Frontiers in Applied Mathematics and Statistics* **3** (2017).

21. K. F. Man, K. S. Tang, S. Kwong, Genetic algorithms: concepts and applications [in engineering design]. *IEEE Transactions on Industrial Electronics* **43**, 519-534 (1996).
22. S. Y. Shin *et al.*, The switching role of β-adrenergic receptor signalling in cell survival or death decision of cardiomyocytes. *Nat Commun* **5**, 5777 (2014).
23. X. Li *et al.*, β-elemene sensitizes hepatocellular carcinoma cells to oxaliplatin by preventing oxaliplatin-induced degradation of copper transporter 1. *Scientific Reports* **6**, 21010 (2016).
24. F. Liu, Y. Shang, S.-z. Chen, Chloroquine potentiates the anti-cancer effect of lidamycin on non-small cell lung cancer cells in vitro. *Acta Pharmacol Sin* **35**, 645-652 (2014).
25. A. Roidl *et al.*, The FGFR4 Y367C mutant is a dominant oncogene in MDA-MB453 breast cancer cells. *Oncogene* **29**, 1543-1552 (2010).
26. N. J. Chew *et al.*, FGFR3 signaling and function in triple negative breast cancer. *Cell Commun Signal* **18**, 13 (2020).
27. M. A. Hatlen *et al.*, Acquired On-Target Clinical Resistance Validates FGFR4 as a Driver of Hepatocellular Carcinoma. *Cancer Discovery* **9**, 1686-1695 (2019).
28. D. Norris *et al.*, Signaling Heterogeneity is Defined by Pathway Architecture and Intercellular Variability in Protein Expression. *iScience* **24**, 102118 (2021).
29. A. Chakrabarty, V. Sanchez, M. G. Kuba, C. Rinehart, C. L. Arteaga, Feedback upregulation of HER3 (ErbB3) expression and activity attenuates antitumor effect of PI3K inhibitors. *Proc Natl Acad Sci U S A* **109**, 2718-2723 (2012).
30. M. Will *et al.*, Rapid induction of apoptosis by PI3K inhibitors is dependent upon their transient inhibition of RAS-ERK signaling. *Cancer Discov* **4**, 334-347 (2014).
31. C. Fedele *et al.*, SHP2 Inhibition Prevents Adaptive Resistance to MEK Inhibitors in Multiple Cancer Models. *Cancer Discov* **8**, 1237-1249 (2018).
32. C. G. Cremers, L. K. Nguyen, Network rewiring, adaptive resistance and combating strategies in breast cancer. *Cancer Drug Resistance* **2**, 1106-1126 (2019).
33. Michael J. Lee *et al.*, Sequential Application of Anticancer Drugs Enhances Cell Death by Rewiring Apoptotic Signaling Networks. *Cell* **149**, 780-794 (2012).
34. J. S. Zawistowski *et al.*, Enhancer Remodeling during Adaptive Bypass to MEK Inhibition Is Attenuated by Pharmacologic Targeting of the P-TEFb Complex. *Cancer Discov* **7**, 302-321 (2017).

35. B. N. Kholodenko, Cell-signalling dynamics in time and space. *Nat Rev Mol Cell Biol* **7**, 165-176 (2006).
36. M. Ghomlaghi, A. Hart, N. Hoang, S. Shin, L. K. Nguyen, Feedback, Crosstalk and Competition: Ingredients for Emergent Non-Linear Behaviour in the PI3K/mTOR Signalling Network. *Int J Mol Sci* **22** (2021).
37. X. Zhao *et al.*, FGFR4 provides the conduit to facilitate FGF19 signaling in breast cancer progression. *Molecular Carcinogenesis* **57**, 1616-1625 (2018).
38. S. Feng *et al.*, Combination treatment of prostate cancer with FGF receptor and AKT kinase inhibitors. *Oncotarget* **8**, 6179 (2017).
39. K. R. Singleton *et al.*, Kinome RNAi screens reveal synergistic targeting of MTOR and FGFR1 pathways for treatment of lung cancer and HNSCC. *Cancer research* **75**, 4398-4406 (2015).
40. R. Turkington *et al.*, Fibroblast growth factor receptor 4 (FGFR4): a targetable regulator of drug resistance in colorectal cancer. *Cell death & disease* **5**, e1046-e1046 (2014).
41. M. A. Ahmed *et al.*, Correction: Fibroblast growth factor receptor 4 induced resistance to radiation therapy in colorectal cancer. *Oncotarget* **10**, 5385 (2019).
42. J. Wang *et al.*, Ligand-associated ERBB2/3 activation confers acquired resistance to FGFR inhibition in FGFR3-dependent cancer cells. *Oncogene* **34**, 2167-2177 (2015).
43. M. T. Herrera-Abreu *et al.*, Parallel RNA interference screens identify EGFR activation as an escape mechanism in FGFR3-mutant cancer. *Cancer discovery* **3**, 1058-1071 (2013).
44. A. Issa *et al.*, Combinatorial targeting of FGF and ErbB receptors blocks growth and metastatic spread of breast cancer models. *Breast Cancer Research* **15** (2013).
45. D. L. Cunningham *et al.*, Differential responses to kinase inhibition in FGFR2-addicted triple negative breast cancer cells: a quantitative phosphoproteomics study. *Sci Rep* **10**, 7950 (2020).
46. A. Prahallad *et al.*, Unresponsiveness of colon cancer to BRAF(V600E) inhibition through feedback activation of EGFR. *Nature* **483**, 100-103 (2012).

FIGURE LEGENDS

Figure 1. Effect of the FGFR4 inhibitor BLU9931 on FGFR4 downstream signalling pathways and proliferation in the MDA-MB-453 cell line. (A) Dose dependent effect of BLU9931 on expression and activation of downstream signalling proteins 1 h post-treatment with the indicated doses. **(B)** Quantification by densitometry of (A). Data were first normalised relative to the actin control, then phosphorylated proteins were normalised to total protein, finally data were expressed relative to DMSO control which was arbitrarily set at 1.0. **(C)** Effect of BLU9931 on proliferation in the FGFR4-positive MDA-MB-453 (upper panel) and FGFR4-negative control MDA-MB-468 cell lines (lower panel). Cell proliferation was determined by direct cell counting. Error bars: mean ± standard error of three biological replicates. ** indicates p-value of < 0.01 and *** < 0.001, comparing individual BLU9931 concentrations to the DMSO vehicle control. **(D)** Time course analysis of BLU9931 on FGFR4 downstream signalling pathways in the MDA-MB-453 cell line. Expression and activation of downstream signalling proteins 1, 4, 8 and 24 h post-treatment with 10 nM of BLU9931. U indicates untreated control, D indicates DMSO vehicle control. Representative of three biological replicates.

Figure 2. Development and calibration of a mathematical model of the FGFR4 signalling network. (A) A simplified schematic diagram depicting the network interactions included in the FGFR4 model, consisting of major RTKs, converging downstream signalling pathways and key feedback and crosstalk mechanisms. A detailed model reaction diagram is provided in Figure S2. The full model reaction rates and ODEs are given in Supplemental Table S1-2. **(B)** Model fitting to experimental data. Comparison of model simulation using best-fitted parameter sets (blue lines, error bars: mean ± standard error, n=5) against experimental time-course and dose-response data (red lines, error bars: mean ± standard error, n=3) demonstrate good agreement between simulation and data. Data used for model calibration were quantified from Figures 1A,D.

Figure 3. Co-inhibition of FGFR4 and AKT, but not PI3K, eliminates pAKT rebound and suppresses MDA-MB-453 cell proliferation. (A-D) Model prediction of phosphorylated AKT (pAKT) dynamics in response to FGFR4 inhibitor BLU9931 and PI3Kα inhibitor BYL719 in single or combination treatment. Error bars: mean ± standard error of five best-fitted parameter sets. **(E)** Dose dependent effect of BLU9931 in combination with BYL719, pan-PI3K inhibitor BKM120 on AKT phosphorylation in the MDA-MB-453 cell line. Activation of AKT was characterized 1 h and 24 h post-treatment with the indicated doses in single or combination treatment. U indicates untreated control, D indicates DMSO vehicle control. **(F)** Quantification by densitometry of data in (E). The quantified data were normalised to DMSO control. **(G, H)** Parental MDA-MB-453 cells were subjected to single inhibitor treatment or combinations of BLU9931 and BYL719 (G) or BKM120 (H). Cell proliferation was determined by MTS assay. Error bars: mean ± standard error of four biological replicates. ** indicates p-value of < 0.01. **(I)** Model prediction of pAKT dynamics in response to FGFR4 and AKT inhibitors in single or combination treatments. To model AKT inhibition, the parameter values associated with AKT catalytic activity were

inhibited by 90%. Error bars: mean ± standard error of five best-fitted parameter sets. **(J)** Dose dependent effect of the FGFR4 inhibitor BLU9931 in combination with AKT inhibitor MK2206 on AKT phosphorylation in the MDA-MB-453 cell line. Activation of AKT was characterized 1 h and 24 h post-treatment with the indicated doses of single or combination treatment. U indicates untreated control, D indicates DMSO vehicle control. **(K)** MDA-MB-453 cells were subjected to single inhibitor treatment or a combination of BLU9931 and MK2206. Cell proliferation was determined by MTS assay. Error bars: mean ± standard error of four biological replicates. * indicates p-value of < 0.05, ** < 0.01, *** < 0.001.

Figure 4. Identification of upregulated RTKs in parental and BLU9931-resistant MDA-MB-453 cells. (A) Model prediction of the dynamic responses of phosphorylated RTKs, predicting they are temporally upregulated following BLU9931 treatment in parental MDA-MB-453 cells. Error bars: mean ± standard error of five best-fitted parameter sets. **(B)** Expression and activation of RTKs and FGFR4 downstream signalling proteins at 1 and 24 h post-treatment with the indicated BLU9931 concentrations in parental MDA-MB-453 cells, compared with long-term (LT) BLU9931 MDA-MB-453 cells. The latter were harvested 24 h post-seeding. **(C-D)** The proliferation of parental and long-term MDA-MB-453 cells treated with DMSO vehicle control, 10 nM (C) or 100 nM BLU9931 (D). Cell proliferation was determined by MTS assay. Error bars: mean ± standard error of six biological replicates. ** indicates p-value of < 0.01, *** < 0.001.

Figure 5. Model prediction of synergistic drug combinations and experimental validation. (A) *In silico* prediction of the effect of 20 possible pair-wise drug combinations co-targeting FGFR4 and various network components, assessed using a drug synergy score (see Materials and Methods for detail). Error bars: mean ± standard error of five best-fitted parameter sets. **(B, C)** Dose dependent effect of Lapatinib on the expression and phosphorylation of ErbB2 in long-term 10 nM (B) or 100 nM BLU9931 MDA-MB-453 cells (C). **(D-G)** Parental (D, E) and long-term 10 nM or 100 nM BLU9931 (F, G) MDA-MB-453 cells were subjected to single inhibitor or combination treatment of BLU9931 and Lapatinib at the indicated doses. Cell proliferation was determined by MTS assay. Error bars: mean ± standard error of three biological replicates. * indicates p-value of <0.05, ** < 0.01, *** < 0.001.

Figure 6. Model-based sensitivity analysis and identification of network architecture controlling pAKT rebound. (A) A 3D plot showing *in silico* simulation of the temporal phosphorylated AKT dynamics in response to FGFR4 inhibition, as each of the model kinetic parameters was inhibited individually (by 75% of the nominal value). The pAKT dynamics of the intact (non-perturbed) model is highlighted in white as control. The pAKT time profiles were averaged across five best-fitted parameter sets. **(B)** Illustration of the general quantitative metrics: *rebound* (RB) and *early drug effect* (EDE) scores, which characterise a typical rebound response, here depicted for the BLU9931-induced pAKT dynamics as an example. These metrics are derived from several basic measures: B: pre-treated (basal) pAKT level; C: the minimal level of pAKT

following drug treatment; and Y: the steady-state level of pAKT after drug treatment. **(C)** Sensitivity analysis results displaying the effect of systematically blocking each of the model kinetic parameters (by reducing the nominal values by 75%) on the RB and EDE scores of the BLU9931-induced pAKT response, relative to the control (no perturbation) condition. **(D)** A hierarchical clustering analysis of the RB and EDE scores obtained in (C), which identifies two major subgroups (group A and B) of the kinetic parameters. The scores are colour coded in log2 scale. **(E)** Simulated time profiles of pAKT response to FGFR4 inhibition when parameters of group A (blue lines) or B (red lines) were blocked, compared to the control (non-perturbed, black line) scenario. Blocking group A's parameters attenuates, while blocking group B's parameters intensifies pAKT rebound. **(F)** A simplified schematic highlighting the network links governed by the kinetic parameters belonging to group A (red lines) and B (blue lines).

Figure 7. Analysis of drug-induced pAKT/pERK response profiles across a large panel of cancer cell types. (A, B) Model prediction of pAKT and pERK time-course profiles in response to FGFR4 inhibition in 350 cancer cell lines using cell-type specific models generated by incorporating protein expression data from CCLE. **(C)** Classification of the cell lines into subgroups based on the response patterns of pAKT and pERK. INC: increase, DEC: decrease, REB: rebound, NOC: no change. **(D, E)** Modelling based identification of network perturbations (i.e. upregulation of the red or downregulation of the blue components) that may convert the pAKT response from a REB to an INC pattern (D); or the pERK response from a REB to a DEC pattern (E), demonstrating the marked plasticity of network-mediated drug response dynamics. **(F)** Time course analysis of treatment using the FGFR4 inhibitor H3B-6527 on FGFR4 downstream signalling pathways in the Hep3B cell line. Expression and activation of downstream signalling proteins were characterized 1, 4, 8 and 24 h post-treatment with 50 nM H3B-6527. U indicates untreated control, D indicates DMSO vehicle control. Representative of three biological replicates. **(G)** Effect of H3B-6527 treatment on proliferation of Hep3B cells. Cell proliferation was determined by MTS assay. Error bars: mean ± standard error of three biological replicates. * indicates p-value of < 0.05, ** < 0.01. **(H)** Parental Hep3B cells were subjected to single inhibitor treatments or a combination of H3B-6527 and Trametinib as indicated. Cell proliferation was determined by MTS assay. Error bars: mean ± standard error of four biological replicates. * indicates p-value of < 0.05, **< 0.01, *** < 0.001.

Figure 1

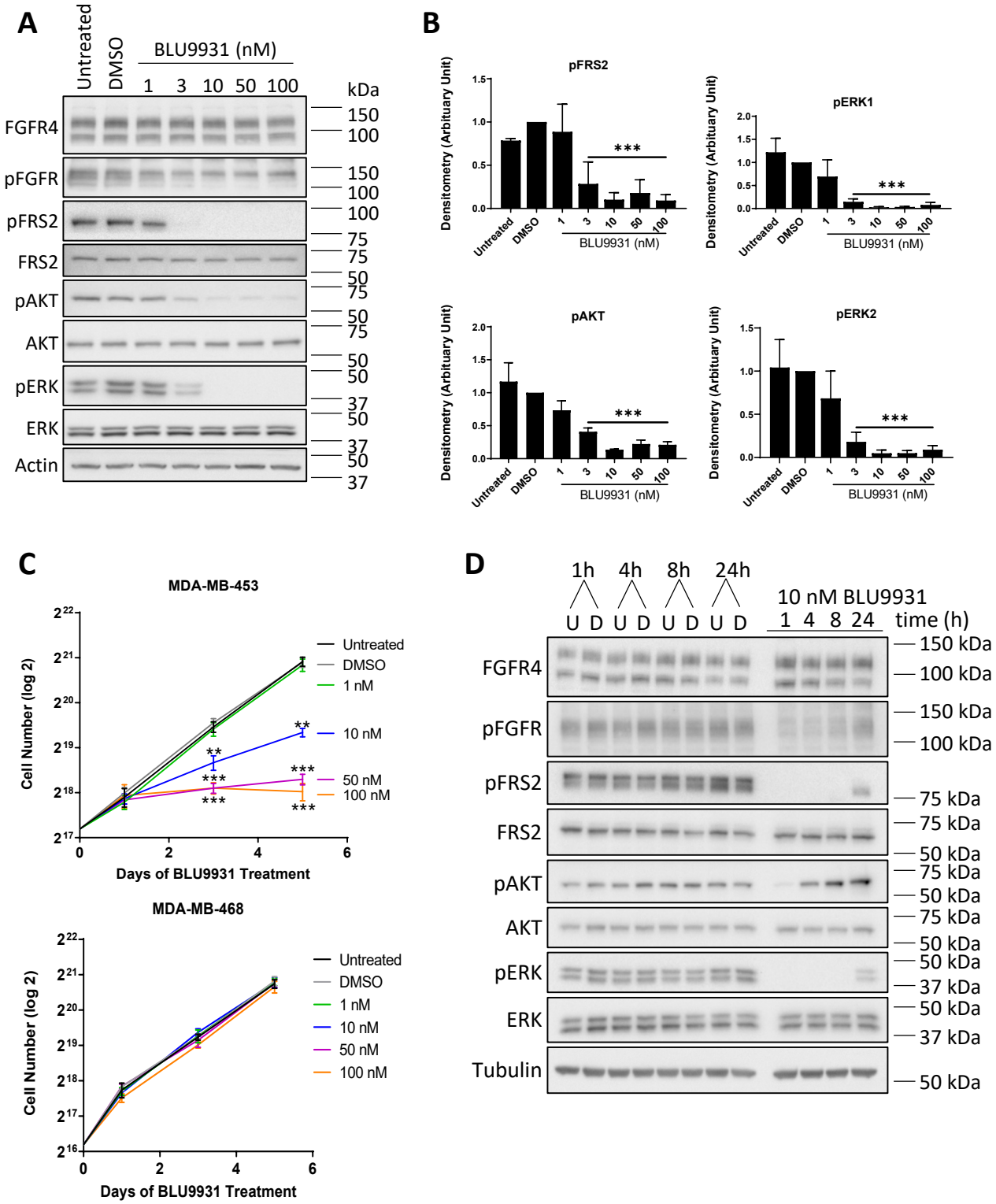

Figure 2

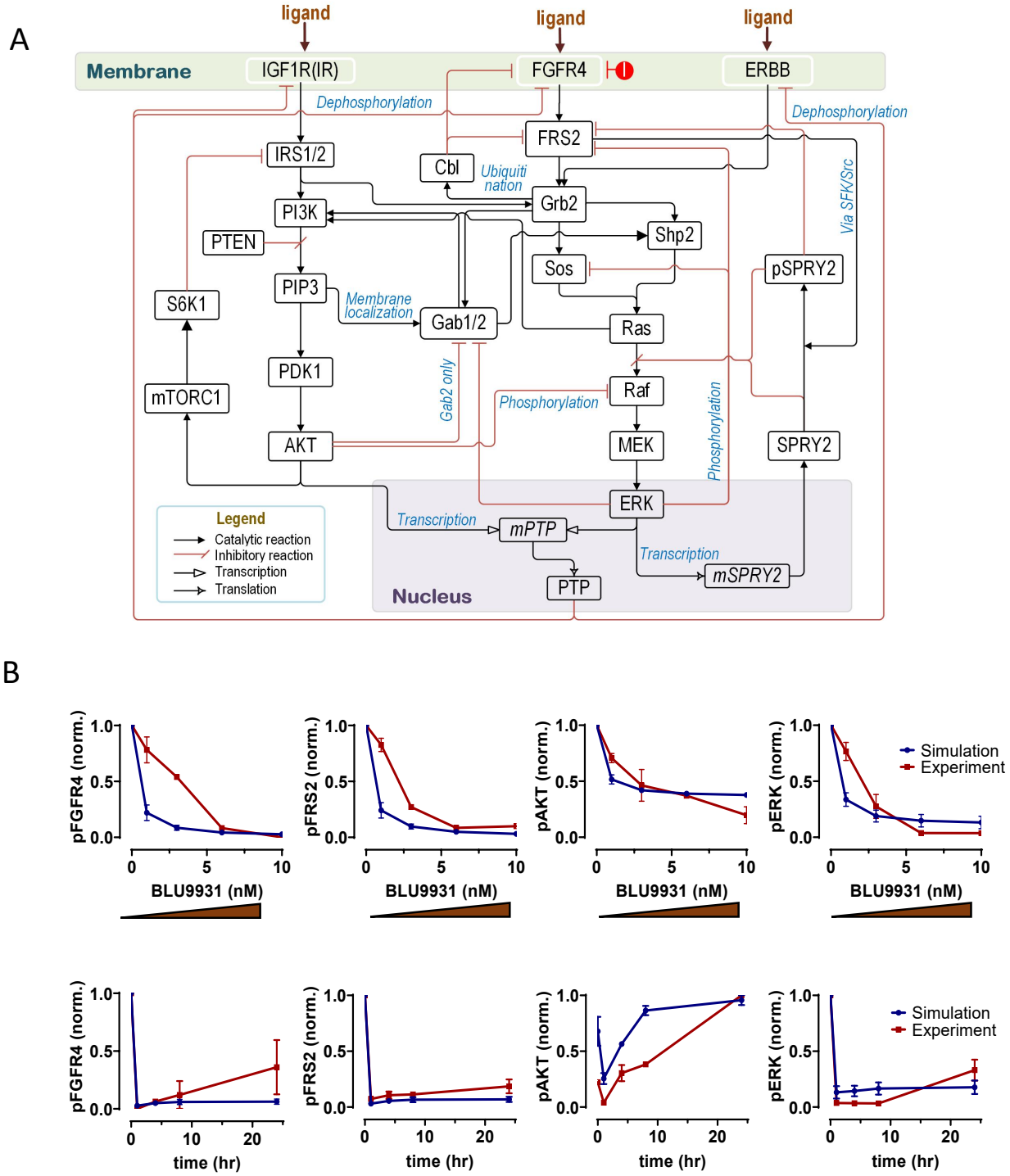

Figure 3

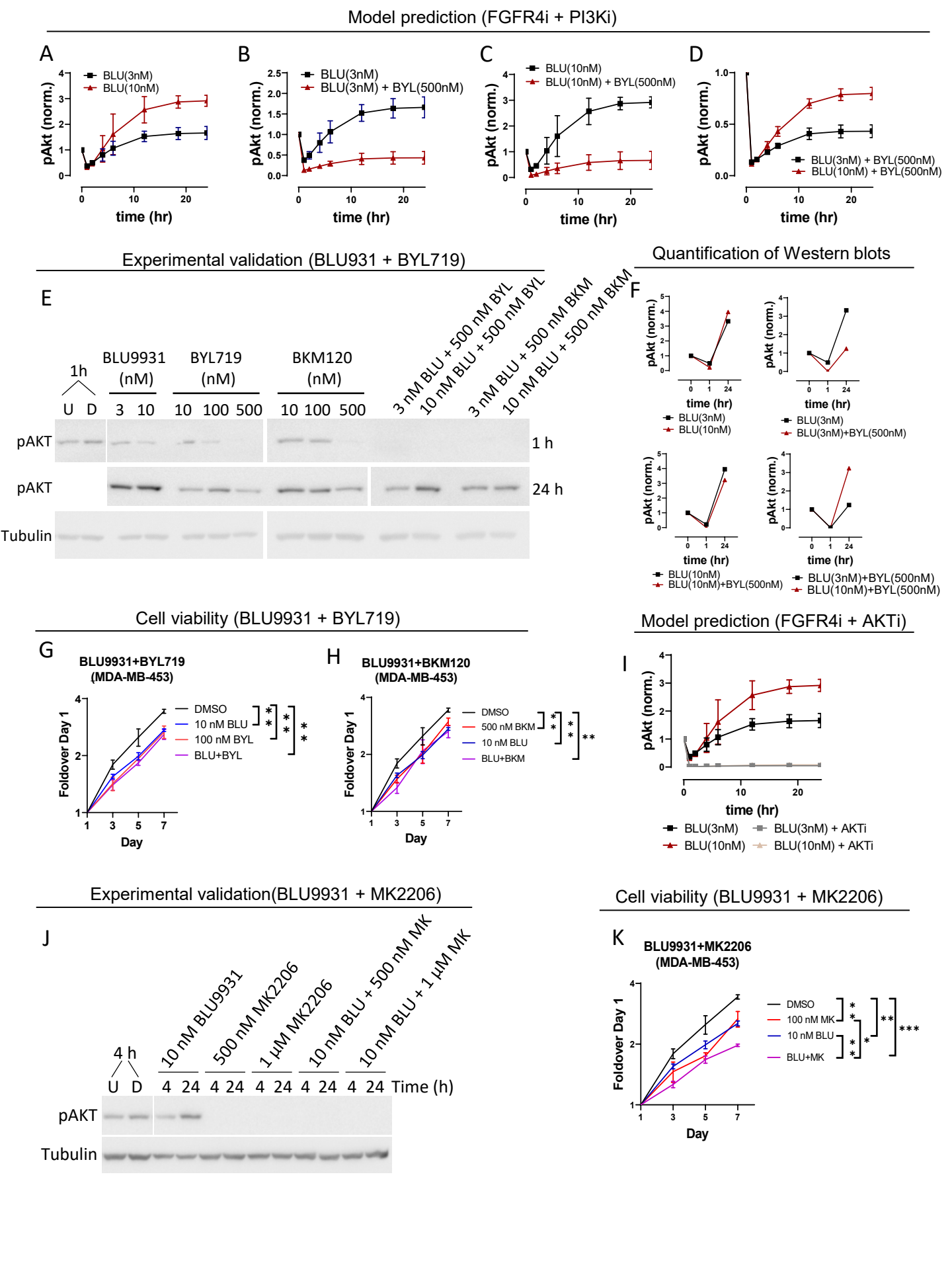

Figure 4

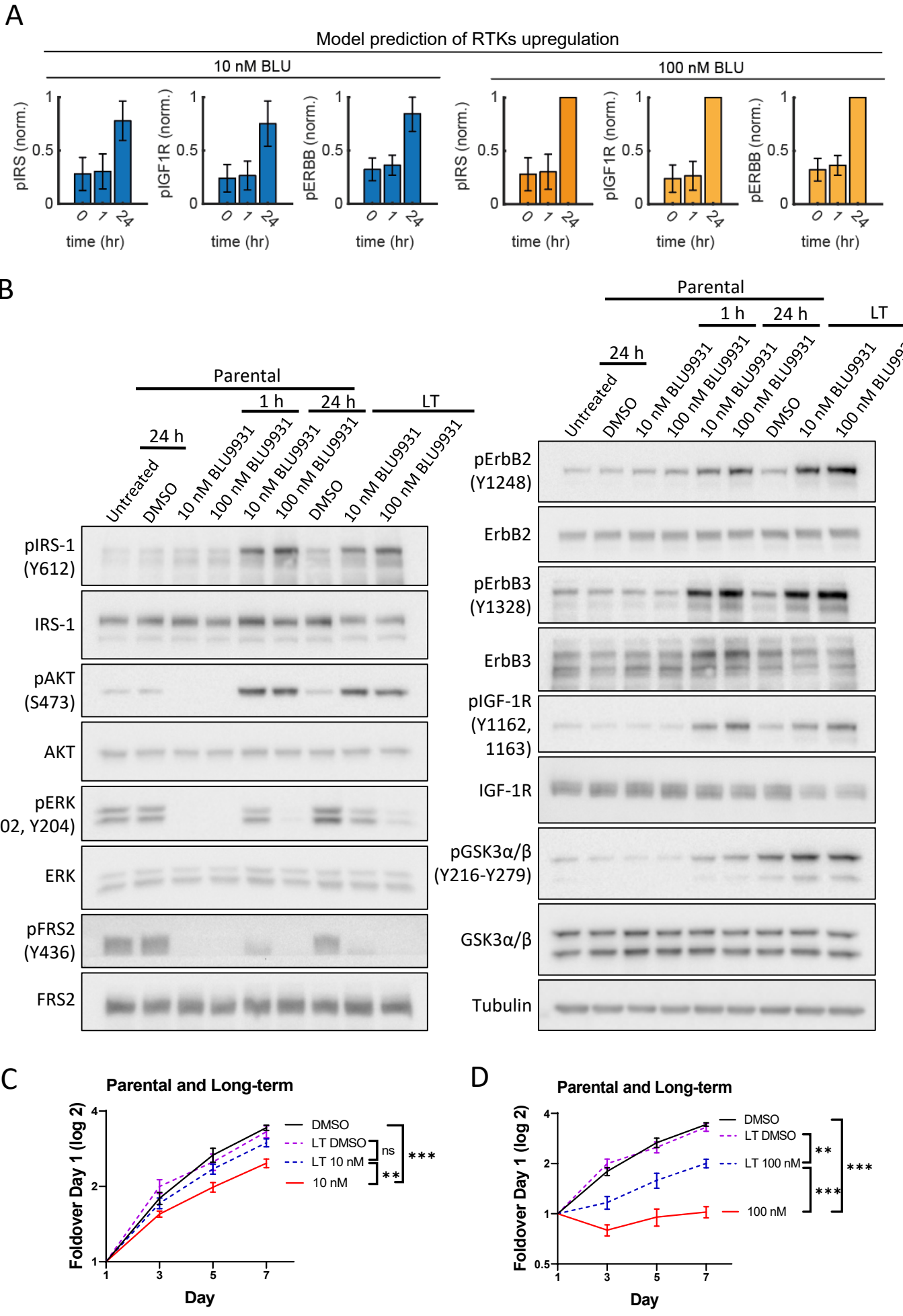

Figure 5

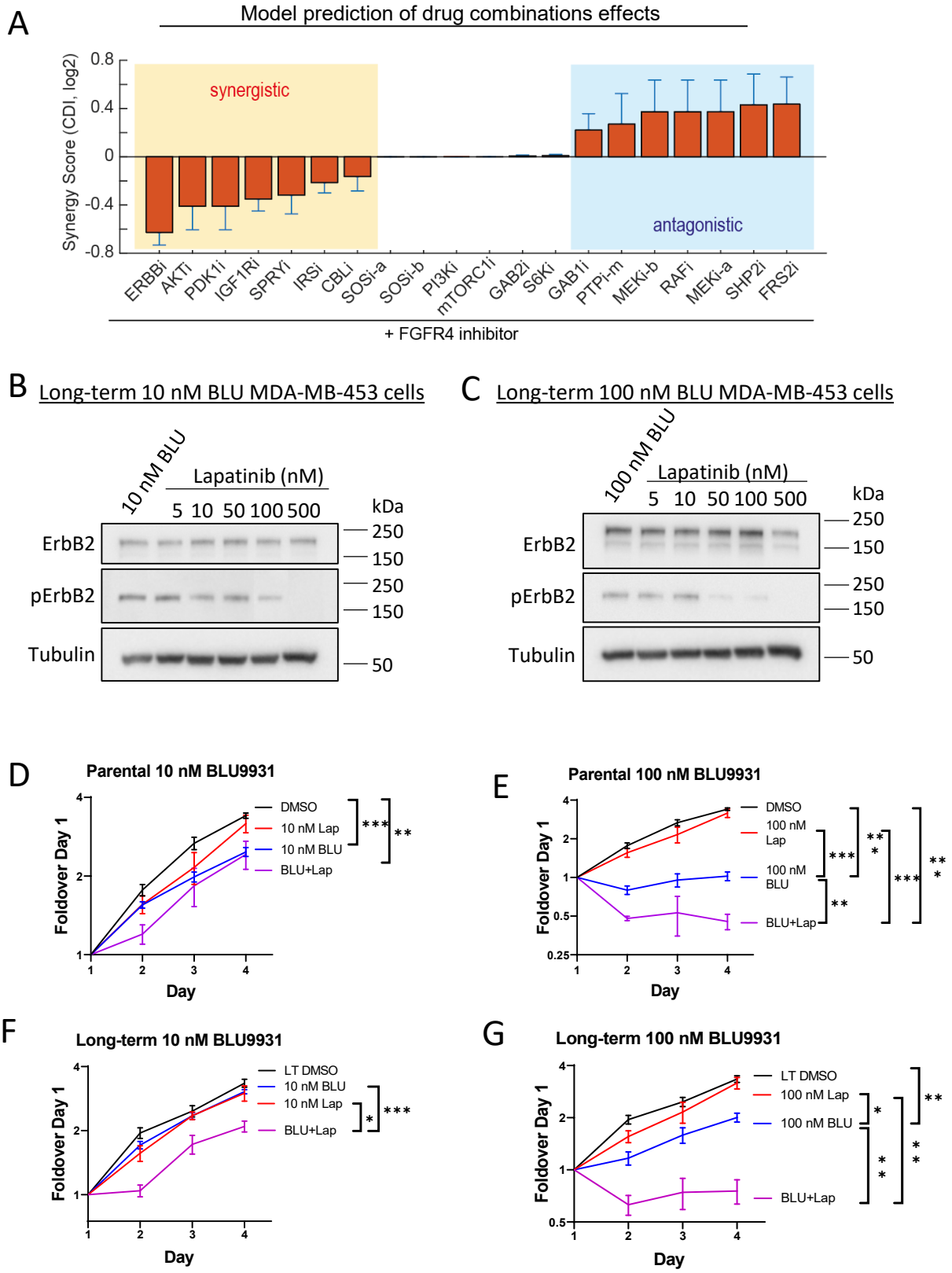

Figure 6

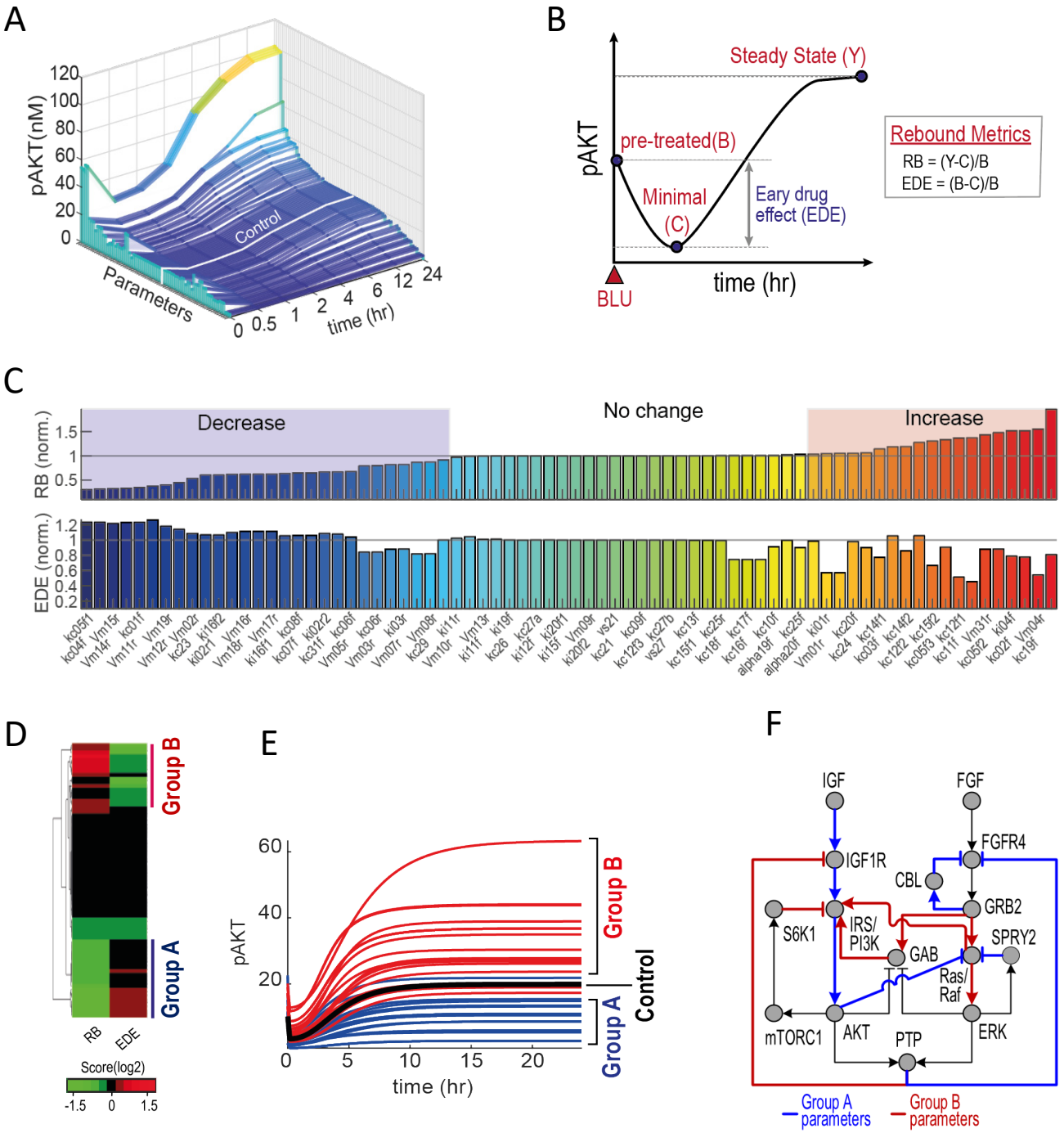

Figure 7